Electrochimica Acta 174 (2015) 682–687

Contents lists available at ScienceDirect

Electrochimica Acta

journal homepage: www.elsevier.com/locate/electacta

Electrochemical performance of single crystal belt-like $NH_4V_3O_8$ as cathode material for lithium-ion batteries

A. Ottmann[a,*], G.S. Zakharova[a,b], B. Ehrstein[a], R. Klingeler[a,c]

[a] Kirchhoff-Institute for Physics, Heidelberg University, INF 227, 69120 Heidelberg, Germany
[b] Institute of Solid State Chemistry, Ural Division, Russian Academy of Sciences, Pervomaiskaya ul. 91, 620990 Yekaterinburg, Russia
[c] Centre for Advanced Materials, Heidelberg University, INF 225, 69120 Heidelberg, Germany

ARTICLE INFO

Article history:
Received 1 April 2015
Received in revised form 27 May 2015
Accepted 7 June 2015
Available online 15 June 2015

Keywords:
Ammonium trivanadate
Hydrothermal synthesis
Belt-like microcrystal
Cathode material
Lithium-ion battery

ABSTRACT

$NH_4V_3O_8$ with belt-like morphology has been synthesized via a hydrothermal process, using acetic acid as acidulant. The resulting phase-pure $NH_4V_3O_8$ microcrystals have smooth surfaces and are typically 25–45 μm long, 2–15 μm wide, and 0.6–1.2 μm thick. Electrochemical studies by means of cyclic voltammetry and galvanostatic cycling show that the pristine material is a suitable host for reversible Li^+ de-/intercalation. Analysis of the peak currents from cyclic voltammetry by means of the Randles-Sevcik equation suggests that the Li^+ de-/intercalation is diffusion-controlled with $D \sim 5 \cdot 10^{-15}\,cm^2\,s^{-1}$. The maximum discharge capacity, at 20 mA g^{-1}, amounts to 299 mA h g^{-1}. At 90 mA g^{-1}, it is still 201 mA hg^{-1} with a capacity retention of 90% in the 100th cycle, indicating the belt-like $NH_4V_3O_8$ being a promising candidate for application as cathode material in secondary lithium-ion batteries.

1. Introduction

Ammonium trivanadate, $NH_4V_3O_8$, has been widely investigated in recent years whereby its potential as cathode material for secondary lithium-ion batteries has been elucidated [1–4]. It has a layered structure similar to LiV_3O_8, which is considered a promising cathode material for lithium-ion batteries as well [5–7]. $NH_4V_3O_8$ has a layered structure composed of two basic structure units (Fig. 1), namely VO_6 octahedrons and VO_5 square pyramids [8,9]. NH_4^+-cations occupy the sites between the vanadium-oxide layers. A network of N-H···O hydrogen bonds between the cationic and polyanionic layers increases the structural stability [1], which is beneficial for the stability and long-term cyclability of electrode materials.

Conventionally, $NH_4V_3O_8$ is synthesized by acidification of a NH_4VO_3 solution with hydrochloric or sulfuric acid and subsequent treatment under hydrothermal conditions [10–12]. More recently, an improved surfactant assisted method with sodium dodecylbenzenesulfonate or sodium dodecylsulfonate was proposed [1,3]. $NH_4V_3O_8 \cdot 0.37H_2O$ nanorods, prepared in the presence of sodium dodecylbenzenesulfonate, demonstrate a maximum specific discharge capacity of 327 mA h g^{-1} at 30 mA g^{-1} and good cycling stability [3]. In comparison, $NH_4V_3O_8 \cdot 0.2H_2O$ flakes, synthesized by using sodium dodecylsulfonate as surfactant, yields discharge capacities of only 177–226 mA h g^{-1} at 15 mA g^{-1} [1]. In addition to shape-controlled synthesis via surfactant assistance, anion doping affects the electrochemical properties of $NH_4V_3O_8$ as well. Torardi et al. [13] have shown that fluoride doped ammonium trivanadate $(NH_4)_{0.9}V_3O_{7.9}F_{0.1} \cdot 0.9H_2O$ has an initial discharge capacity of 409 mA h g^{-1} at a very low scanrate of ~5 mA g^{-1}, but exhibits poor cycle life. Low electronic conductivity, which is an issue for applicability of ammonium trivanadate as a battery material, can be improved by adding highly conductive material, for instance carbon nanotubes (CNT). This is demonstrated by $NH_4V_3O_8$/CNT composite with flake-like morphology which exhibits high discharge capacities of up to 359 mA h g^{-1} at 30 mA g^{-1} as well as excellent cycling stability [2]. In general, carbon coating is the most suitable tool to overcome the drawback of low intrinsic electronic conductivity in the case of electrode materials such as olivine-structured phosphates [14,15].

Recently, we have described a facile hydrothermal method to produce $NH_4V_3O_8$ with controlled shape and morphology, including shuttles, flowers, belts, and plates [16]. The electrochemical properties of the pristine material with belt-likemorphology, synthesized that way, are reported in the present work, including analysis of cyclic voltammetry by means of the Randles-Sevcik equation. This analysis suggests diffusion-controlled Li^+ transport in the active material with $D \sim 5 \cdot 10^{-15}\,cm^2\,s^{-1}$. Galvanostatic cycling implies a maximum discharge capacity of 299 mA h g^{-1} (at 20 mA g^{-1}) and a capacity retention of 90% in the 100th cycle (at

* Corresponding author.
E-mail address: alex.ottmann@kip.uni-heidelberg.de (A. Ottmann).

http://dx.doi.org/10.1016/j.electacta.2015.06.027
0013-4686/

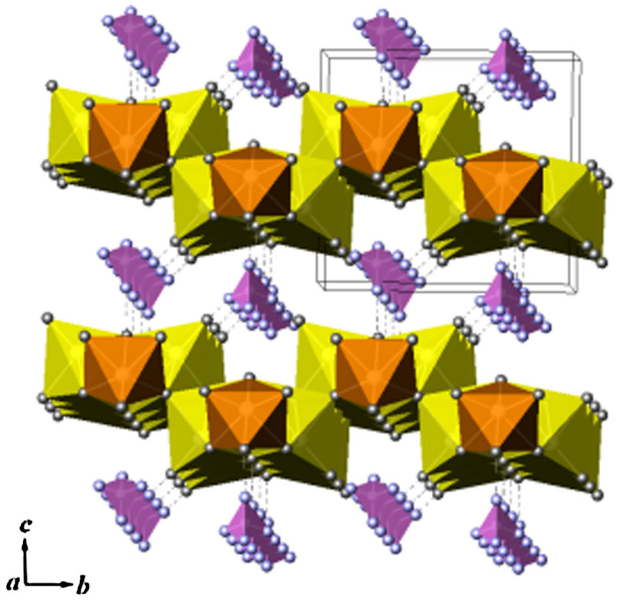

Fig. 1. The structure of $NH_4V_3O_8$ viewed along the *a* axis, showing the twisted zigzag layers of VO_5 and VO_6 in yellow and brown, respectively. The NH_4^+ groups are located in the interlayer space [8] (For interpretation of the references to color in this figure legend, the reader is referred to the web version of this article.).

90 mA g^{-1}), indicating the belt-like microcrystals being a promising candidate for lithium-ion batteries.

2. Experimental

$NH_4V_3O_8$ microbelts have been prepared via a hydrolysis reaction under hydrothermal conditions. Ammonium metavanadate (NH_4VO_3, Sigma-Aldrich) was used as vanadium source. Glacial acetic acid (100% CH_3COOH, VWR Chemicals) was used as hydroscopic substance and to adjust the pH value of the reaction solution. A typical synthesis procedure proceeds as follows: 0.2 g NH_4VO_3 is dissolved in 20 ml deionized water. Afterwards, an appropriate amount of acetic acid is added drop-wise under stirring to the initially clear-orange solution to adjust the pH value to about 4. The resulting wine-red solution is transferred into a teflon-lined stainless steel autoclave, kept at 140 °C for 48 h and finally cooled down to room temperature naturally. Then, the obtained precipitation is collected by centrifugation, washed and dried at 60 °C for 8 h.

The product was characterized by powder X-ray diffraction (XRD) by means of a Bruker AXS D8 ADVANCE ECO using Cu Kα radiation (λ = 0.15418 nm) with a step size of $\Delta 2\theta = 0.02°$. The final refinement of structural parameters was done by a full-profile analysis using the FullProf-2010 software. The morphology of the powder was determined by scanning electron microscopy (Nano-SEM, FEI). The specific surface area and pore volume of the sample were measured by a surface area and porosity analyzer (Gemine VII, Micromeritics).

Electrochemical measurements by means of cyclic voltammetry and galvanostatic cycling were performed by a VMP3 potentiostat (BioLogic), while the cells were held at 25 °C in a climate chamber [17]. The working electrodes were prepared from a mixture of pristine $NH_4V_3O_8$ powder, carbon black (Timcal) and polyvinylidenefluoride binder (Solvay Plastics) in a weight ratio of 80:15:5. The binder was dissolved in N-methyl-2-pyrrolidone (NMP, Sigma-Aldrich) under stirring. Then, the $NH_4V_3O_8$ material and carbon black were added and the mixture was stirred overnight. After evaporating most of the NMP at ~80 °C, the resultant slurry was spread on a circular Al-mesh, dried overnight at 100 °C in vacuum, mechanically pressed at 10 MPa and dried again. The two-electrode Swagelok-type cells were assembled in a glove box with Ar-atmosphere ($O_2/H_2O < 1$ ppm). A lithium metal foil disk (Alfa Aesar) pressed on a nickel current collector was used as counter electrode. Both electrodes were separated by two layers of glass microfibre (Whatman GF/D), which was soaked with 200 μl electrolyte (Merck Electrolyte LP30), a 1 mol dm^{-3} solution of $LiPF_6$ in 1:1 ethylene carbonate (EC) and dimethyl carbonate (DMC).

3. Results and discussion

Fig. 2a shows the X-ray diffraction pattern of the as-prepared powder. All peaks can be indexed in a monoclinic lattice system with space group $P2_1/m$. The calculated lattice parameters of $NH_4V_3O_8$ are $a = 0.4975(8)$ nm, $b = 0.8413(14)$ nm, $c = 0.7855(6)$ nm, $\beta = 96.39(6)°$, $V = 0.3267(1)$ nm^3, which are similar to the ones from JCPDS card no. 088-1473 [8]. The large relative intensity of the (0 0 1) diffraction peak indicates good crystallinity and preferred orientation of the powder sample [1,18]. The as-prepared material is mainly composed of single microcrystals with well-defined faces

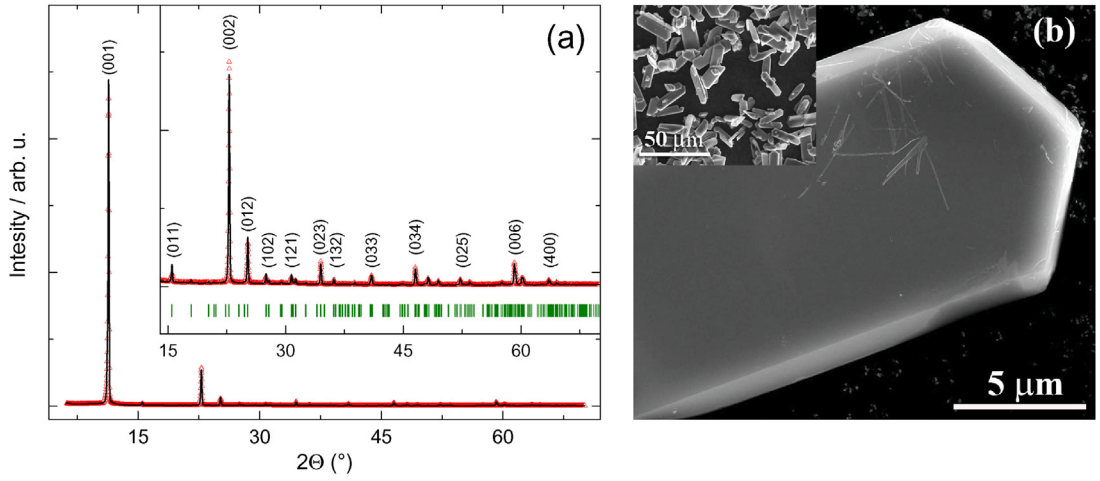

Fig. 2. (a) XRD pattern of as-prepared $NH_4V_3O_8$ powder (red triangles) and full-profile analysis (black line) based on JCPDS card no. 088-1473 [8]. Diffraction peaks are indexed according to space group $P2_1/m$. (b) Representative SEM images of the as-prepared material showing the belt-like shape of the microcrystals (For interpretation of the references to color in this figure legend, the reader is referred to the web version of this article.).

as seen in in Fig. 2b. The width and thickness of the microbelts are in the range of 2–15 μm and 0.6–1.2 μm, respectively, with a typical length of 25–45 μm (Fig. 2b, inset). According to our previous thermogravimetric investigation [16], the pristine $NH_4V_3O_8$ contains 0.35 mol crystal water per formula unit ($NH_4V_3O_8 \cdot 0.35H_2O$) and is thermally stable up to 344 °C.

Chemical reactions which might occur during the $NH_4V_3O_8$ formation can be listed as follows:

$$NH_4VO_3 + H_2O \rightarrow HVO_3 + NH_4OH \quad (1)$$

$$4HVO_3 + H_2O \rightarrow VO_3^- + H_3O^+ \quad (2)$$

$$CH_3COOH + H_2O \rightarrow CH_3COO^- + H_3O^+ \quad (3)$$

$$2VO_3^- + 2H^+ \leftrightarrow V_2O_5 + H_2O \quad (4)$$

$$3V_2O_5 + 2NH_4OH \rightarrow 2NH_4V_3O_8 + H_2O \quad (5)$$

When NH_4VO_3 and acetic acid are added into deionized water, the hydrolysis reactions (1)–(4) occur. The reversibility of reaction (4) depends on the pH value of the solution. After adding acetic acid as acidulant, the reaction's (4) equilibrium drifts to the right and favors the formation of V_2O_5 [19]. Subsequently, reaction (5) would mainly take place and $NH_4V_3O_8$ is synthesized. Dissociating in water, acetic acid produces CH_3COO^- and H^+ ions. The H^+ ions change the pH of the solution to the required value pH = 4. The CH_3COO^- ions can act as a monodentate ligand. This ligand could play a crucial role in the formation of the single $NH_4V_3O_8$ microcrystals with belt-like morphology as in contrast adding mineral acid yields flake-like particles [1,12].

The described chemical synthesis route of the $NH_4V_3O_8$ microbelts is schematically shown in Fig. 3. In the initial stage of the reaction, crystal nuclei are formed through the hydrolysis of NH_4VO_3. During heating in the autoclave, the nuclei grow to form small particles of $NH_4V_3O_8$. With increasing reaction time, bigger particles evolve from capturing smaller ones by the so-called Ostwald ripening process [20].

The BET surface area of the obtained $NH_4V_3O_8$ microbelts amounts to $1.77 \pm 0.03\ m^2\ g^{-1}$ and the pore volume is $4 \cdot 10^{-4}\ cm^3\ g^{-1}$.

The $NH_4V_3O_8$ microcrystals were characterized electrochemically by means of cyclic voltammetry and galvanostatic cycling with potential limitation (GCPL). Fig. 4 shows the 1st and 5th cycle of a cyclic voltammogram (CV) obtained at a scan rate of $0.05\ mV\ s^{-1}$ in the range of 1.0–4.0 V. During the 1st cycle, starting with the cathodic sweep at an open cell voltage of 3.1 V, three main reduction peaks around 1.65, 2.44 and 2.87 V and two main

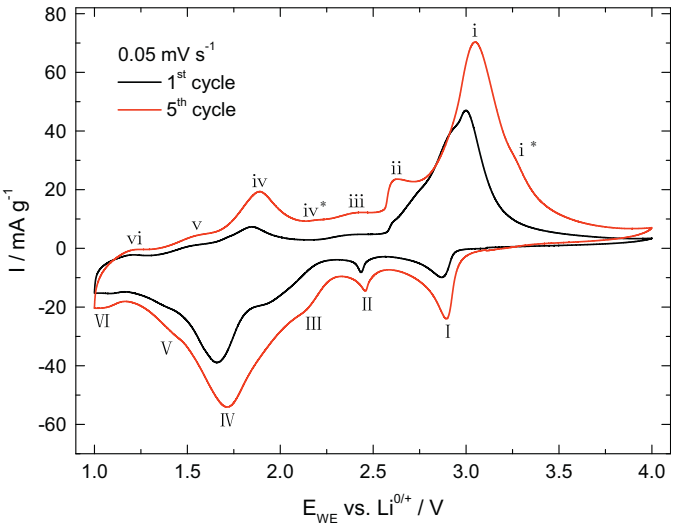

Fig. 4. The 1st and 5th CV cycle of single crystalline $NH_4V_3O_8$ microbelts, measured at a scan rate of $0.05\ mV\ s^{-1}$. Roman numbers label six cathodic and eight anodic features (see the text).

oxidation peaks around 1.85 and 3.00 V are observed. The details of the redox features become more distinguishable with advancing cycle number, which is represented in the 5th cycle where six cathodic (I–VI) and eight anodic features (i–vi, i*, iv*) can be identified (see Fig. 4). The main reason for an increase of the overall electrochemical activity during the first cycles is associated with an initial strong electrode polarization, which diminishes in the course of several cycles [1]. The observed redox peaks can be attributed to de-/intercalation of Li^+-ions from/into the $NH_4V_3O_8$ structure [1], which is accompanied by redox activity of $V^{5+/4+}$ and potentially $V^{4+/3+}$.

For comparison, two initial charge/discharge curves recorded at a specific current of $10\ mA\ g^{-1}$ with potential limits of 1.0 and 4.0 V are plotted in Fig. 5. In the 1st and 2nd half cycles, specific charge/discharge capacities of 215/261 mA h g^{-1} and 260/275 mA h g^{-1} are reached. Higher capacities in the 2nd cycle agree with the observation of stronger peak currents when comparing the same cycles in the CV. Likewise, both depicted discharge curves show three distinct plateau-like features, which correspond to the main reduction peaks in the CV (Fig. 4), while during the charge process only two plateaus can be distinguished clearly (Fig. 5). Both the CV and the GCPL data imply that the synthesized $NH_4V_3O_8$ microbelts provide a suitable host structure for reversible Li^+ de-/intercalation in the studied potential range, which has been concluded for other

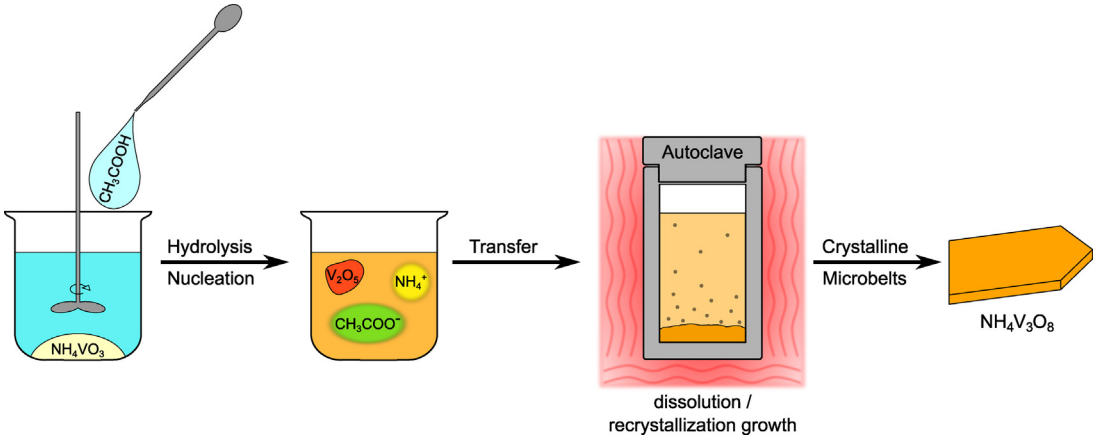

Fig. 3. Chemical synthesis route of $NH_4V_3O_8$ microbelts.

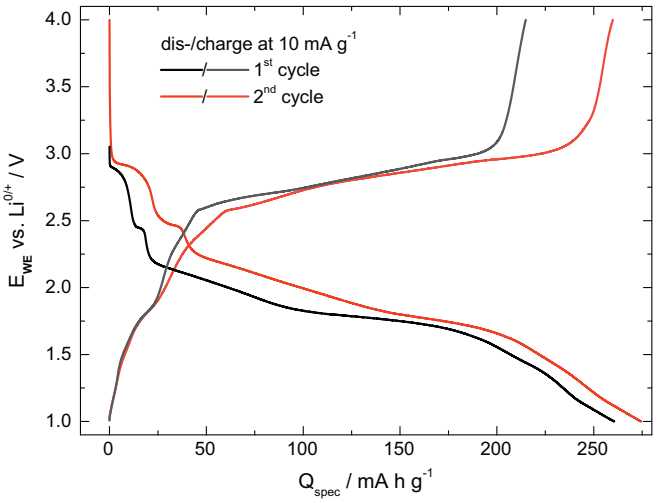

Fig. 5. Charge/discharge curves on $NH_4V_3O_8$ microbelts obtained at 10 mA g^{-1}.

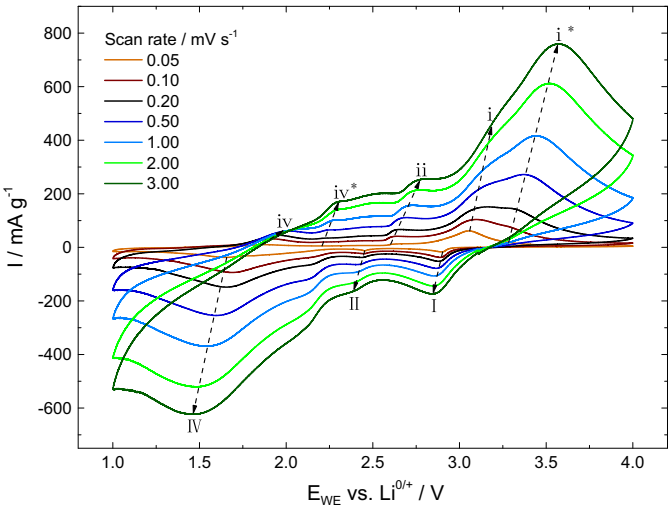

Fig. 7. Cyclic voltammograms of single crystalline $NH_4V_3O_8$ microbelts, measured at different scan rates of 0.05 to 3 mV s^{-1}. Arrows indicate the positions of distinct features upon oxidation ($i^{(*)}$, ii, $iv^{(*)}$) and reduction (I, II, IV) (see the text).

$NH_4V_3O_8$ materials as well [1,3,4,11]. Multiple redox peak pairs in the CV and several plateaus during galvanostatic charge/discharge, respectively, indicate a stepwise de-/intercalation process, whose details and explicit electrochemical reactions remain unclear because of a complex configuration of the crystal structure. The redox active vanadium ions, initially V^{5+}, occupy octahedrally and square-pyramidally coordinated lattice sites [8,9] and referring to $Li_{1+x}V_3O_8$ there are different intercalation sites for the Li^+-ions, too [7,21,22]. So far, there are no studies which are able to assign the individual redox features to distinct electrochemical processes.

Fig. 6 illustrates the evolution of charge/discharge capacities during GCPL measurements in order to evaluate the rate capability (a) and the cycle life (b) of the $NH_4V_3O_8$ microbelts. The cycle life test was performed at a constant charge/discharge current of 90 mA g^{-1} between 1.0 and 4.0 V, while the rate capability measurement contains 2 cycles at 10 mA g^{-1}, 5 cycles at 20 mA g^{-1}, and 10 cycles at 50, 100, 200, and 500 mA g^{-1} with the same potential limits. Both data sets show (within segments of constant current) significantly increasing charge/discharge capacities for roughly 20 (a) and 40 (b) cycles, respectively, with can be associated to the impact of initial electrode polarization. During the cycle life test, a maximum discharge capacity of 201 mA h g^{-1} is reached in the 42nd cycle and 90% of it is maintained in the 100th cycle, what can be valued as stable cycling behavior after some kind of activation. The number of cycles of initial capacity increase is much larger and the effect is more pronounced than, e.g., in Ref. [1] where the maximum capacity is reached after 12 cycles. One may attribute this to a combination of comparably large particle dimensions and good crystallinity of our sample. It has been shown in the example of $Li_{1+x}V_3O_8$ that a high degree of crystallinity hinders electrochemical activity [18,23]. To be specific, $Li_{1+x}V_3O_8$-based electrodes show higher rate capabilities and longer cycle lives for amorphous as compared to single crystalline material [23].

The rate capability measurements confirm the given values with discharge capacities around 195 mA h g^{-1} at 100 mA g^{-1}. Furthermore, they show noticeable capacity losses when increasing the charge/discharge current. To be specific, doubling the charge/discharge current leads to a ~50 mA h g^{-1} lower specific capacity, which results in steady charge/discharge capacities of still as large as ~75 mA h g^{-1} at 500 mA g^{-1}. At 20 mA g^{-1}, a maximum discharge capacity of 299 mA h g^{-1} is reached. As de-/intercalation

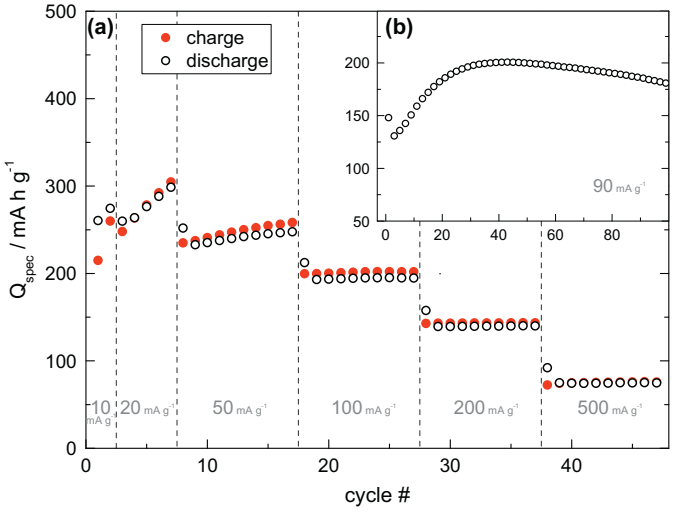

Fig. 6. Specific gravimetric capacity of $NH_4V_3O_8$ microbelts as a function of the cycle number upon cycling at different specific charge/discharge currents. Illustration of (a) rate capability and (b) cycle life.

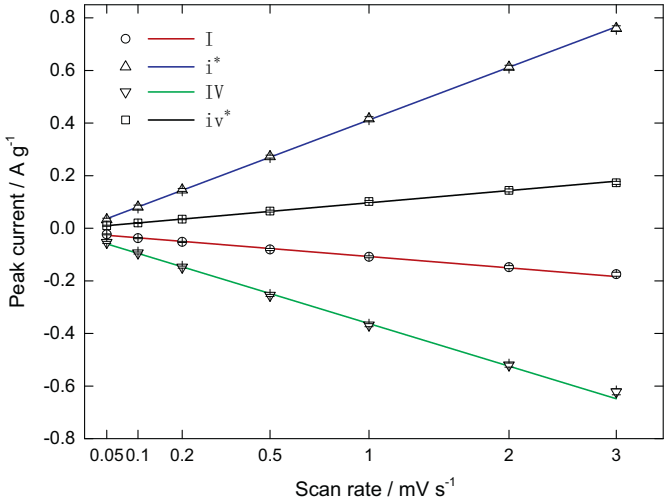

Fig. 8. Peak current of pronounced anodic and cathodic features (I, i^*, IV, and iv^* in Fig. 4). Lines are fits by means of the Randles-Sevcik equation (Eq. (6)).

Table 1
Comparison of the discharge capacity obtained after the 10th, 30th, 50th and 100th cycle and of the diffusion coefficient (obtained by the abovementioned Randles-Sevcik analysis of CVs and by electrochemical impedance spectroscopy EIS) for $NH_4V_3O_8$ with various morphologies as studied in this work as well as in Refs. [1–3], and [11]. In columns 3–5, the relative amount of added carbon black and PVDF, and the used potential range and current rate are listed for each material.

Ref.	Morphology	active:C:PVDF	Potential range (V vs. $Li^{0/+}$)	Current rate ($mA\,g^{-1}$)	Discharge capacity 10th/30th/50th/100th ($mA\,h\,g^{-1}$)	Diffusion coefficient ($cm^2\,s^{-1}$)
This work	microbelts	80:15:5	1.0–4.0	90	155/197/200/182	$5{\cdot}10^{-15}$ (Randles-Sevcik)
[1]	microflakes	85:10:5	1.8–4.0	15	218/210/-/-	–
[2]	microflakes	80:10:10	1.5–4.0	150	197/207/205/172	$3{\cdot}10^{-13}$ (EIS)
[3]	nanorods	80:10:10	1.5–4.0	150	220/233/233/-	–
[11]	nanorods (agglomerated)	80:10:10	1.5– 4.0	15	239/217/-/-	–

of 1 Li^+/f.u. corresponds to a specific capacity of $90\,mA\,h\,g^{-1}$, this result implies that more than 3 Li^+/f.u. can be reversibly de-/intercalated into the $NH_4V_3O_8$ host structure. Correspondingly, the average valency of the vanadium ions is +3.9 at maximum discharge, which suggests that the $V^{4+/3+}$ redox couple takes part in the electrochemical processes. In summary, the data show that the studied microbelts compare well to previous results in literature on similar $NH_4V_3O_8$ materials [1,3,11].

In order to obtain further insight into the lithium de-/intercalation behavior of $Li_xNH_4V_3O_8$, cyclic voltammetry at different scan rates ranging from 0.05–3.00 $mV\,s^{-1}$ was performed. After a set of 6 cycles at 0.05 $mV\,s^{-1}$, 3 cycles of each of 6 further scan rates were recorded in ascending order. One exemplary cycle (5th for 0.05 $mV\,s^{-1}$, 2nd for any other) of each scan rate is shown in Fig. 7. Overall, all peak current intensities increase with increasing scan rate. Compared to the results at 0.05 $mV\,s^{-1}$, which have been discussed by means of Fig. 4, the oxidation peaks marked with i^* and iv^* become more dominant features of the anodic sweep with increasing scan rate (Fig. 7). At lower scan rates those peaks are nearly completely overlain by other features of the CV. In order to evaluate the variation of peak currents depending on the scan rates, the maximum current intensities of the main redox peaks (I, $i^{(*)}$, II, ii, IV, $iv^{(*)}$) were determined graphically, and the variations between different cycles of a particular scan rate were taken into account by adequate error bars. The result of this analysis is depicted in Fig. 8 for peaks I, i^*, IV and iv^*, where a linear dependency between the peak current intensities and the square root of the scan rate is revealed. This relation can be described by the Randles-Sevcik equation (at 25 °C) for diffusion controlled processes [24]:

$$I_p = k \times n^{3/2} A[C]\sqrt{D}\sqrt{v} \quad (6)$$

with peak current I_p, constant k, number of exchanged electrons n, electrode surface area A, bulk concentration of charge carriers $[C]$, diffusion coefficient D, and scan rate v.

The observed linear dependence of the peak currents as a function of $\sqrt{v}$ suggests that the process is indeed diffusion controlled in the studied scan rate range. This result strongly indicates that the electrochemical activity of $NH_4V_3O_8$ is governed by a stepwise diffusive Li^+-ion de-/intercalation process. Surprisingly, the respective reduction and oxidation peaks of redox pairs I/$i^{(*)}$ and IV/$iv^{(*)}$ do not show the same slope in the $I_p(\sqrt{v})$ plot (see Fig. 8). Instead, the reduction/oxidation peak intensities of I/iv^* and IV/i^* depend in approximately the same way on $\sqrt{v}$. Assuming a constant Li^+ diffusion coefficient, there are two possible explanations of this behaviour: (1) The accessible Li^+ (site) concentration ($[C]$) changes during the course of the CV sweeps, and (2), more than one electron could be involved in one of the redox ;1; reactions IV or i^*, which itself may be an artefact of the contribution of other redox processes in close-by potential windows (III, V, and i). This situation introduces serious uncertainty factors for quantitatively determining the Li^+ diffusion coefficient in $NH_4V_3O_8$ by applying the Randles-Sevcik equation. To give an estimation nonetheless, we assume for reduction I a one-electron reaction ($n = 1$) with 1 Li^+/f.u. ($[C] = 10\,mol\,l^{-1}$). Together with the experimentally measured specific surface area of the microbelts ($A = 1.77\,m^2\,g^{-1}$) this yields $D \sim 5{\cdot}10^{-15}\,cm^2\,s^{-1}$. Note that the computed value is very sensitive to the assumptions made, one of which is the applicability of the reversible one-step Randles-Sevcik model. The estimated diffusion coefficient is substantially lower than the one ($3{\cdot}10^{-13}\,cm^2\,s^{-1}$) published in [2], which was determined by electrochemical impedance spectroscopy, and for several $Li_{1+x}V_3O_8$ systems [25–27]. The latter is expected as the NH_4^+-ions occupy interlayer sites, which may hinder Li^+ diffusion in comparison to $Li_{1+x}V_3O_8$ [1,8].

Table 1 illustrates electrochemical properties for materials of different morphology by comparing the results obtained for the microbelts at hand with the literature. As mentioned above, the large region of initially increasing charge/discharge capacities in case of the studied microbelts is consistent with a high degree of crystallinity in the materials. In general, nanorods with the smallest particle dimensions exhibit the highest discharge capacities [3,11]. However, agglomeration seems to reduce the cycling stability significantly as in Ref. [11] the capacity decreases by about 10% between cycle numbers 10 and 30. Note that the very low current rate in Ref. [11] hinders to directly compare the discharge capacities, which is also the case for Ref. [1]. Independent of the particular shape and synthesis procedure, all microstructured materials show similar capacities at intermediate cycling rates. Concerning the cyclic stability, the microbelts studied in the present work maintain 90% of the maximum discharge capacity in the 100th cycle obtained at $90\,mA\,g^{-1}$ which is slightly superior to the microflakes in Ref. [2] with a corresponding value of 83% measured at a current rate of $150\,mA\,g^{-1}$.

5. Conclusion

In summary, $NH_4V_3O_8{\cdot}0.35H_2O$ with a new belt-like morphology has been prepared by a simple acetic acid assisted hydrothermal approach. XRD and SEM results indicate that the obtained material is pure phase. The microbelts have a hexagon outline with an average length of 25–45 μm, width of 2–15 μm, and thickness of 0.6–1.2 μm. The as prepared $NH_4V_3O_8$ electrodes show a good cycling stability with a maximum discharge capacity of 299 $mA\,h\,g^{-1}$ at $20\,mA\,g^{-1}$. At $90\,mA\,g^{-1}$, a maximum discharge capacity of $201\,mA\,h\,g^{-1}$ is reached in the 42nd cycle and 90% of it is maintained in the 100th cycle. The peak currents of pronounced reduction and oxidation peaks in the CVs linearly depend on the square root of the scan rate which according to the Randles-Sevcik equation indicates a diffusion controlled Li^+ de-/intercalation

process in the scan rate range under study. Quantitatively, the analysis yields an estimated Li^+ diffusion coefficient of $\sim 5 \cdot 10^{-15}$ $cm^2 s^{-1}$.

Acknowledgements

This work was supported by the Deutsche Forschungsgemeinschaft through grant KL 1824/7, by the Excellence Initiative of the German Federal Government and States as well as by the Russian Foundation for Basic Research (project 13-03-00146) and the Ministry of Education and Science of the Russian Federation (project 14.613.21.0002). Technical support by I. Glass is gratefully acknowledged.

References

[1] H. Wang, K. Huang, S. Liu, C. Huang, W. Wang, Y. Ren, Electrochemical property of $NH_4V_3O_8 \cdot 0.2H_2O$ flakes prepared by surfactant assisted hydrothermal method, J. Power Sources 196 (2011) 788–792.
[2] H. Wang, K. Huang, Y. Ren, X. Huang, S. Liu, W. Wang, $NH_4V_3O_8$/carbon nanotubes composite cathode material with high capacity and good rate capability, J. Power Sources 196 (2011) 9786–9791.
[3] H. Wang, Y. Ren, W. Wang, X. Huang, K. Huang, Y. Wang, S. Liu, $NH_4V_3O_8$ nanorod as a high performance cathode material for rechargeable Li-ion batteries, J. Power Sources 199 (2012) 315–321.
[4] H. Fei, X. Wu, H. Li, M. Wei, Novel sodium intercalated $(NH_4)_2V_6O_{16}$ platelets: High performance cathode materials for lithium-ion battery, Journal of Colloid and Interface Science 415 (2014) 85–88.
[5] N.A. Chernova, M. Roppolo, A.C. Dillon, M.S. Whittingham, Layered vanadium and molybdenum oxides: batteries and electrochromics, J. Mater. Chem. 19 (2009) 2526–2552.
[6] A. Pan, J. Liu, J.-G. Zhang, G. Cao, W. Xu, Z. Nie, X. Jie, D. Choi, B.W. Arey, C. Wang, S. Liang, Template free synthesis of LiV_3O_8 nanorods as a cathode material for high-rate secondary lithium batteries, J. Mater. Chem. 21 (2011) 1153–1161.
[7] G. Pistoia, S. Panero, M. Tocci, R.V. Moshitev, V. Manev, Solid solutions $Li_{1+x}V_3O_8$ as cathodes for high rate secondary Li batteries, Solid State Ionics 13 (1984) 311–318.
[8] S.D. Huang, Y. Shan, $NH_4V_3O_8$: a novel sinusoidal layered compound formed by the cationtemplating effect, Chem. Commun. 106 (1998) 1069–1070.
[9] B.-Z. Lin, S.-X. Liu, Ammonium trivanadate(V), $NH_4V_3O_8$, Acta Crystallographica C55 (1999) 1961–1963.
[10] L.Q. Mai, C.S. Lao, B. Hu, J. Zhou, Y.Y. Qi, W. Chen, E.D. Gu, Z.L. Wang, Synthesis and Electrical Transport of Single-Crystal $NH_4V_3O_8$ Nanobelts, J. Phys. Chem. B 110 (2006) 18138–18141.
[11] S.-S. Cao, J.-F. Huang, H.-B. Ouyang, L.-Y. Cao, J.-Y. Li, J.-P. Wu, A simple method to prepare $NH_4V_3O_8$ nanorods as cathode material for Li-ion batteries, Materials Letters 126 (2014) 20–23.
[12] D. Vernardou, M. Apostolopoulou, D. Louloudakis, N. Katsarakis, E. Koudoumas, Hydrothermal growth and characterization of shape-controlled $NH_4V_3O_8$, New J. Chem. 38 (2014) 2098–2104.
[13] C.C. Torardi, C.R. Miao, New Battery Cathode Materials: Synthesis, Characterization, and Electrochemical Performance of $M_{(1-x)}V_3O_{(8-y)}F_{(z)} \cdot nH_2O$ (M = NH_4, K), Chem. Mater. 14 (2002) 4430–4433.
[14] K. Zaghib, A. Mauger, C.M. Julien, Overview of olivines in lithium batteries for green transportation and energy storage, J Solid State Electrochem 16 (2012) 835–845.
[15] H. Li, H. Zhou, Enhancing the performances of Li-ion batteries by carbon-coating: present and future, Chem. Commun. 48 (2012) 1201–1217.
[16] G.S. Zakharova, C. Täschner, T. Kolb, C. Jähne, A. Leonhardt, B. Büchner, R. Klingeler, Morphology controlled $NH_4V_3O_8$ microcrystals by hydrothermal synthesis, Dalton Trans. 42 (2013) 4897–4902.
[17] G.S. Zakharova, C. Jähne, A. Popa, C. Täschner, T. Gemming, A. Leonhardt, B. Büchner, R. Klingeler, Anatase Nanotubesas an Electrode Material for Lithium-Ion Batteries, J. Phys. Chem. C 116 (2012) 8714–8720.
[18] G.Q. Liu, C.L. Zeng, K. Yang, Study on the synthesis and properties of LiV_3O_8 rechargeable lithium batteries cathode, Electrochimica Acta 47 (2002) 3239–3243.
[19] J. Livage, Synthesis of polyoxovanadates via chimiedouce, Coordination Chemistry Reviews 178–180 (1998) 999–1018.
[20] W. Ostwald, Über die vermeintliche Isomerie des roten und gelben Quecksilberoxyds und die Oberflächenspannung fester Körper, Zeitschrift für Physikalische Chemie 34 (1900) 495–503.
[21] S. Panero, M. Pasquali, G. Pistoia, Rechargeable $Li/Li_{1+x}V_3O_8$ Cells, J. Electrochem. Soc. 130 (1983) 1225–1227.
[22] N. Dupré, J. Gaubicher, D. Guyomard, C.P. Grey, 7Li and 51V MAS NMR Study of the Electrochemical Behavior of $Li_{1+x}V_3O_8$, Chem. Mater. 16 (2004) 2725–2733.
[23] G. Pistoia, M. Pasquali, G. Wang, L. Li, $Li/Li_{1+x}V_3O_8$ Secondary Batteries: Synthesis and Characterization of an Amorphous Form of the Cathode, J. Electrochem. Soc. 137 (1990) 2365–2370.
[24] R.S. Nicholson, I. Shain, Theory of Stationary Electrode Polarography: Single Scan and Cyclic Methods Applied to Reversible, Irreversible, and Kinetic Systems, Analytical Chemistry 36 (1964) 706–723.
[25] F. Wu, L. Wang, C. Wu, Y. Bai, Structural characterization and electrochemical performance of lithium trivanadate synthesized by microwave sol–gel method, Electrochimica Acta 54 (2009) 4613–4619.
[26] J. Kawakita, T. Miura, T. Kishi, Lithium insertion and extraction kinetics of $Li_{1+x}V_3O_8$, J. Power Sources 83 (1999) 79–83.
[27] H. Heli, H. Yadegari, A. Jabbari, Investigation of the Lithium Intercalation Behavior of Nanosheets of LiV_3O_8 in an Aqueous Solution, J. Phys. Chem. C 115 (2011) 10889–10897.